Linking pore-scale interfacial curvature to column-scale capillary pressure

Ryan T. Armstrong [a,*], Mark L. Porter [b], Dorthe Wildenschild [a]

[a] School of Chemical, Biological, and Environmental Engineering, Oregon State University, 103 Gleeson Hall Corvallis, OR 97331-2702, United States
[b] Los Alamos National Laboratory, Earth and Environmental Sciences Division, Los Alamos, NM 87545, United States

ARTICLE INFO

ABSTRACT

Synchrotron-based tomographic datasets of oil–water drainage and imbibition cycles have been analyzed to quantify phase saturations and interfacial curvature as well as connected and disconnected fluid configurations. This allows for close observation of the drainage and imbibition processes, assessment of equilibrium states, and studying the effects of fluid phase disconnection and reconnection on the resulting capillary pressures and interfacial curvatures. Based on this analysis estimates of capillary pressure calculated from interfacial curvature can be compared to capillary pressure measured externally with a transducer. Results show good agreement between curvature-based and transducer-based measurements when connected phase interfaces are considered. Curvature measurements show a strong dependence on whether an interface is formed by connected or disconnected fluid and the time allowed for equilibration. The favorable agreement between curvature-based and transducer-based capillary pressure measurements shows promise for the use of image-based estimates of capillary pressure for interfaces that cannot be probed with external transducers as well as opportunities for a detailed assessment of interfacial curvature during drainage and imbibition.

© 2012 Elsevier Ltd. All rights reserved.

1. Introduction

Capillary pressure (P_c) is inherently a pore-scale phenomenon and is defined at equilibrium as the difference in pressure across a curved interface separating two immiscible fluids, expressed as

$$P_c = P_{nw} - P_w \tag{1}$$

where P_{nw} is the non-wetting phase pressure at an interface and P_w is the wetting phase pressure at an interface (wetting and non-wetting phases are defined below). In a multiphase system, P_c is attributable to the normal component of the interfacial forces at the interfacial boundaries. By considering a small segment of a curved interface, balancing pressure and interfacial forces, and assuming static equilibrium, the Young-Laplace equation can be written as

$$P_c = 2\sigma\kappa \tag{2}$$

where σ is the interfacial tension between the wetting and the non-wetting phase and κ is mean curvature. For example, if applying Eq. (2) to a simple capillary tube geometry, assuming the interface is spherical, κ is defined as

$$\kappa = \cos(\alpha)/r \tag{3}$$

where α is the contact angle (measured as the angle between the fluid–fluid interface and the solid surface) and r is the radius of the capillary tube. When measuring α through a given phase, the phase is considered wetting for $\alpha < 90°$ and non-wetting for $\alpha > 90°$. However, for more complex systems the combined effect of contact angle and pore morphology on κ is not easily defined and direct measurement of κ is usually unfeasible for opaque media.

Traditionally, capillary pressure is defined at the macro-scale by the following empirical relationship

$$P^{nw} - P^w = P^c(S^w) \tag{4}$$

where for a given elementary representative volume (REV), P^{nw} is the average nonwetting phase pressure, P^w is the average wetting phase pressure, P^c is the macroscopic capillary pressure, and S^w is wetting phase saturation. This traditional approach assumes that P^c is a function of saturation only; other pore-scale properties, such as interfacial configuration, interfacial curvature, contact angle, and pore morphology are ignored. The previously mentioned properties tend to be lumped into S^w without consideration of their individual effects. Ultimately, this oversimplification of the pore-scale physics, during drainage and/or imbibition, results in a non-unique solution for P^c.

Using a thermodynamic approach, Hassanizadeh and Gray [7,8] and Gray and Hassanizadeh [2,3] and more recently Gray and Miller [4] stressed the importance of including interfacial properties when modeling multiphase flow at the macro-scale. The general concept in their approach has been to develop a model that explicitly accounts for the interfaces in a multiphase system. They propose that the traditional macroscale $P^c(S^w)$ function does not

---

* Corresponding author.
   E-mail address: ryan.armstro@gmail.com (R.T. Armstrong).

fully account for all of the pore scale physics and that an additional term, specific interfacial area (a^{nw}), is needed [7,8,4]. The following functional relationship for capillary pressure was proposed

$$P^c = P^c(S^w, a^{nw}) \qquad (5)$$

With the inclusion of a^{nw} in the macro-scale capillary pressure relationship, Hassanizadeh and Gray [8] hypothesized that all possible static P^c values lie on a unique surface and that the hysteretic effect seen with Eq. (4) is simply an artifact of projecting a 3D surface onto the P^c–S^w plane. A few experimental and numerous modeling results have shown that a unique P^c–S^w–a^{nw} surface exists for a given pore morphology, suggesting that the inclusion of a^{nw} provides a unique solution for P^c, or at least removes most of the hysteretic effect [19,5,1,10,17,16]. However, pore network modeling results from Helland and Skjaeveland [6] show that contact angle hysteresis can result in a non-unique solution for Eq. (5). Contact angle hysteresis was studied by Liu et al. [11], for a single smooth-walled channel, and their results demonstrate that even though inclusion of interfacial area in the capillary pressure saturation relationship reduces hysteresis, interfacial area is directly dependent on contact angle and thus is not an independent variable. At the macroscale S^w and a^{nw} may parameterize the small scale physics, as reported in the numerous reports cited above, such that contact angle does not appear in the macroscale equation (Eq. (5)). However, understanding the dependency of larger-scale parameters (e.g. specific interfacial area) on pore-scale parameters (e.g. contact angle) is critical when evaluating the constitutive functional relationship for P^c and further work is needed in this area to fully understand these dependencies.

More recently, dynamic effects in capillary pressure have been studied, and it is well accepted that the rate of change of saturation must be considered [9,12,14,13]. While the rate of change of saturation is an important parameter, Gray and Miller [4] show that changes in interfacial area densities must also be included when considering dynamic effects that impact capillary pressure. However, very little experimental evidence has been presented that addresses the relaxation and/or rearrangement of interfaces during the transition from dynamic to static conditions. Despite the fact that such experimental evidence is prerequisite for assessing the time needed for equilibration, and thus, the circumstances required to warrant use of an equilibrium assumption. Additionally, no experimental evidence has been presented in the literature that addresses the additional dynamic effect of interfacial rearrangement at constant saturation proposed by Gray and Miller [4].

Our approach to quantifying capillary pressure evolution is to investigate interfacial curvature measured from computed X-ray microtomography (CMT) images obtained during imbibition and drainage experiments. In the collected images, fluids were separated into 4 individual fluid configurations: (1) connected wetting, (2) disconnected wetting, (3) connected non-wetting, and (4) disconnected non-wetting. We compare the average interfacial curvature for the interfaces separating the connected phases (i.e. fluid configurations 1 and 3) to capillary pressure measured with an external pressure transducer. Average mean curvature is then used in the Young-Laplace equation (Eq. (2)) to calculate an average curvature-based capillary pressure ($\langle P_c \rangle$). This approach allows for a direct comparison between capillary pressure calculated from a pore-scale interfacial property (i.e. curvature) and column-scale capillary pressure measured using a pressure transducer.

Pragmatically, the two pressure measurement approaches are different. A pressure transducer evaluates P^c according to Eq. (4), where P^{nw} is generally measured at the column outlet using a hydrophobic membrane, and P^w is generally measured at the column inlet using a hydrophilic membrane. The disadvantage to this measurement technique is that P^c is not related to any sort of inter-

facial property and S^w is averaged over the whole column assuming saturation gradients are small. Conversely, $\langle P_c \rangle$ calculated from curvature using the Young–Laplace equation (Eq. (2)) directly considers an "intrinsic" interfacial property, i.e., curvature [8]. This distinction is crucial, because it is unclear how pressure transducer-based measurements account for disconnected fluid interfaces and how the transducer averages P_c over the entire column. In essence, an external pressure (transducer) measurement is some volume averaged value. In our opinion, it is critical to understand how well this value represents pore-scale interfacial curvature. Assuming that interfacial curvature can be accurately measured from pore-scale CMT data, the CMT-based approach used herein could provide significant improvement in the evaluation of macro-scale capillary pressure.

To the best of our knowledge, this report is the first direct experimental comparison between micro-scale P_c measured via interfacial curvature and macro-scale P^c measured via a pressure transducer in a 3D porous medium. A few attempts have been made using other imaging techniques in 2D micromodels, Cheng et al. [1] and Pyrak-Nolte et al. [18] measured interfacial curvature in 2D from microscope images using a level set approach and found a reasonable correlation between transducer measured P^c and interfacial curvature. Additionally, Liu et al. [11] measured interfacial curvature from confocal laser scanning microscopy images by fitting the interfaces to the arc of a circle. Ultimately, the accuracy of a given curvature measurement depends on the quality of the original image, where both image resolution and the signal-to-noise ratio are critical. Herein, we validate our curvature measurement method by testing it against CMT images of precision glass spheres and CMT images of capillary tube menisci, and lastly, we compare pore-scale interfacial curvature measurements to column-scale capillary pressure measurements during drainage and imbibition.

2. Materials and methods

2.1. Experimental setup

In this work, we further analyze CMT data for the drainage and imbibition experiments reported by Porter et al. [16]. These experiments were conducted at the GeoSoilEnviro Consortium for Advanced Radiation Sources (GSECARS) bending magnetic beamline, Sector 13, Advanced Photon Source (APS), Argonne National Laboratory. The experimental system consisted of soda-lime glass beads (35% 0.6 mm diameter, 35% 0.8 mm diameter, and 30% 1.0–1.4 mm diameter) packed in a 25.0 mm long glass column with an inside diameter of 7.0 mm (see Supporting Material 1). A semi-permeable, hydrophilic membrane was placed at the bottom of the column to prevent the non-wetting phase (Soltrol 220, $\rho = 0.79$ g/cm^3, $\sigma = 0.0378$ N/m) from entering the water line. A rubber stopper containing the non-wetting phase outlet line was placed inside the column in contact with the top of the porous medium. The wetting phase consisted of potassium iodide doped water (1:6 mass ratio of KI:H$_2$O) and the amount of wetting phase pumped in and out of the column was precisely controlled (±1 μl) by a syringe pump (Gilson 402). In the present work, where the focus is on minute details, i.e., local curvature-based estimates of P_c, the saturation values are based on the imaged sub-section analyzed for curvature, whereas in Porter et al. [16] the saturations were estimates for the entire column and thus based on the pumped volumes (see Supporting Material 2 for a comparison of these two alternative saturation measurements). The pressure of each phase was measured (Validyne P55 Differential Pressure Transducer) in the fluid lines above and below the porous medium. A point on the P^c–S^w curve was obtained by pumping a precise amount of wetting phase into

(imbibition) or out of (drainage) the column at a flow rate of 0.6 ml/hr, turning off the pump, allowing the fluids to equilibrate for 10–15 min (equilibration times were determined by the time limitation at the beam line), and then imaging a 5.5 mm section of the column at 13 μm/pixel resolution. In a few cases fluid movement was observed in the CMT images (noticeable by the blurring and/or streaking of the reconstructed image) after 10–15 min and the system was allowed to equilibrate until no fluid movement was observed. Thus, it was assumed that the points on the P^c–S^w curve had reached near-equilibrium conditions. The column was initially fully saturated with the wetting phase and primary drainage (PD), main imbibition (MI), main drainage (MD), secondary imbibition (SD), and secondary drainage (SD) curves were measured in succession.

2.2. Image segmentation

To accurately identify the solid and two fluid phases the reconstructed gray-scale CMT images obtained from the APS require further image processing. Typically, the images are filtered to remove random noise, and then segmented so that each phase is identified by a single integer. The segmented data was first filtered with an edge preserving anisotropic diffusion filter and then segmented with a k-means clustering algorithm. Further details regarding the segmentation algorithm and its validation can be found in Porter and Wildenschild [15].

Representative elementary volume (REV) analysis for S^w and a^{nw} was conducted ([16], Fig. 3) to ensure that the size of the analyzed cube (128.6 mm^3) provides meaningful results when volume averaged. However, interfacial curvatures were not considered in Porter et al. [16], and thus further REV qualification is needed in this report. To resolve this issue a larger cylindrical volume (194.7 mm^3) was extracted from the segmented data and analyzed for curvature. The larger cylindrical volume gave nearly identical curvature results to that measured from the smaller cubed volume (see Supporting Material 3). Thus, for simplicity in data processing (less memory and CPU required), the smaller cube (128.6 mm^3) was used for the analyses presented herein.

2.3. Image analysis: connectivity

Segmented images were analyzed for connectivity throughout the assigned REV. An algorithm in Avizo Fire® called Reconstruct was used to rebuild an image starting from markers placed at the top and bottom of the segmented volume. The algorithm exclusively retrieves objects in the image space that are connected to the set markers, using a 26 neighborhood voxel-connectivity requirement (see Avizo Fire® documentation for more information). To reflect the experimental setup, a marker for the oil phase was placed at the top REV slice and a marker for the water phase was placed at the bottom REV slice. Thus, any oil phase voxel connected to the top slice was retrieved and considered to be connected. Likewise, any water phase voxel connected to the bottom slice was retrieved and considered to be connected. Using this approach the assigned REV was segregated into 4 fluid configurations: (1) connected wetting, (2) disconnected wetting, (3) connected non-wetting, and (4) disconnected non-wetting. An example image is provided in Supporting Material 4.

2.4. Image analysis: interfacial curvature

The first step of the curvature calculation process was to construct isosurfaces from the segmented images. Isosurfaces were generated between the following fluid configurations: connected wetting/connected non-wetting, connected wetting/disconnected non-wetting, and disconnected wetting/connected non-wetting,

using a surface generating marching cube algorithm in Avizo Fire®. The surfaces are smoothed using a $4 \times 4 \times 4$ kernel applying sub-voxel weights such that the surface is naturally smoothed. However, no labels are modified, meaning that any two voxel centers that were labeled differently prior to smoothing remain separated by the generated surface afterwards.

Curvature was approximated locally on the triangulated interfacial surface by the equation commonly used to describe a quadratic form

$$ax^2 + by^2 + cz^2 + 2exy + 2fyz + 2gzx + 2lx + 2my + 2nz + d = 0 \quad (6)$$

where the parameters are optimized during approximation. The eigenvalues and eigenvectors of the quadratic form correspond to the principal curvature values and to the directions of principal curvature, respectively. This produces a surface scalar field that contains the mean value of the two principal curvature values, i.e., mean curvature (κ), as used in Eq. (2). Once the surface is functionalized, the curvature measurement algorithm in Avizo Fire® called GetCurvature, is used to calculate mean curvature (κ) as the mean of the two principal curvatures, κ_1 and κ_2

$$\kappa = (\kappa_1 + \kappa_2)/2 \quad (7)$$

To smooth the curvature distribution data, mean curvature values that corresponded to adjacent triangular elements were averaged over a common neighborhood. Only triangles sharing a common edge and/or corner are considered common neighbors. The curvature estimation method was tested on artificial CMT data for a meniscus in a capillary tube, real CMT data for a meniscus in a capillary tube, and CMT images of precision glass spheres (0.8 mm ± 0.1 mm).

The artificial CMT capillary meniscus data were generated with a code[1] written in C++ that uses the analytical expression for a curved meniscus in a capillary tube to generate a 3D single-precision floating point array that represents a realistic geometry. The input parameters are: capillary tube diameter, curvature, amplitude of the Gaussian noise signal, and number of pixels in the x, y, and z directions. The artificial data were generated to have similar phase separation and noise as the actual CMT images collected during our experiments, and this was accomplished primarily by adjusting the Gaussian noise signal. Example histograms of both artificial and real CMT data are provided in Supporting Material 5. Curvature was constrained by a 25° contact angle. The contact angle was evaluated experimentally by placing a droplet of Soltrol oil on a glass slide submerged in water. The resulting contact angle was computed using ImageJ based on B-spline active contours [20]. Lastly, this algorithm allowed us to vary the capillary tube radius to represent the range of P_c values expected during the drainage and imbibition experiments.

Capillary meniscus data was also generated experimentally by placing a capillary tube in a (sealed) water reservoir, letting KI-doped water rise in the tube, allowing for equilibrium, and then imaging with CMT. Mean curvature was calculated from the CMT image and compared to the analytical solution (Eq. (3)). A third additional validation was performed by measuring curvature on a CMT image of precision glass spheres (0.8 mm ± 0.1 mm).

3. Results and discussion

3.1. Curvature validation

The artificial CMT capillary meniscus data was generated to represent the range of capillary pressure values measured via the pressure transducer during the drainage and imbibition

---

[1] Courtesy of James McClure (University of North Carolina).

experiments. Fig. 1 shows the relative percent difference (RPD), calculated as the percent difference between the true and measured interfacial curvature relative to the average value of both measurements (i.e. $\{[\text{measured} - \text{true}]/[[\text{true} + \text{measured}]/2]\} * 100$), encountered using this approach for the range of P_c values analyzed. Fig. 1a demonstrates that as P_c increases, error increases. This trend is essentially a resolution problem caused by pixelation (see Fig. 1b which is in terms of pixel radius instead of P_c). As P_c increases, the capillary tube radius decreases, and thus, the number of pixels representing an interface decreases and error is accrued.

Since P_c values encountered in these experiments range from 100 Pa to 300 Pa, Fig. 1 suggests that, based on the artificial meniscus data, the largest error encountered should be ~10%. To support this error estimate, a partially saturated capillary tube was imaged with CMT and the curvature of the meniscus was measured. The mean curvature (i.e. P_c) was found to be within 3.3% relative difference from the analytical solution, and the relative difference estimated from Fig. 1 is 3.0%. Thus, the error versus P_c relationship (Fig. 1) using the artificial CMT data is supported by experimental data. An additional validation was performed by measuring curvature on a CMT image of precision glass spheres. The measured radius of curvature for this dataset was found to be within 5% of the true bead radius (0.8 mm ± 0.1 mm per manufacturer's specifications).

Fig. 2 presents an example of curvature values measured from a single CMT volume of the connected wetting fluid interfaces. A convex interface is negative in the water phase, meaning that for water-wet media only negative curvatures should exist. However, the curvature distributions have a tail of unrealistic positive curvature values (Fig. 2). After further analysis of the segmented images, it was discovered that the positive values are caused by segmentation error, which improperly reverses the curvature of very small interfaces (see above discussion related to pixelation issues). Interfaces that form pendular rings and interfaces located at pore necks
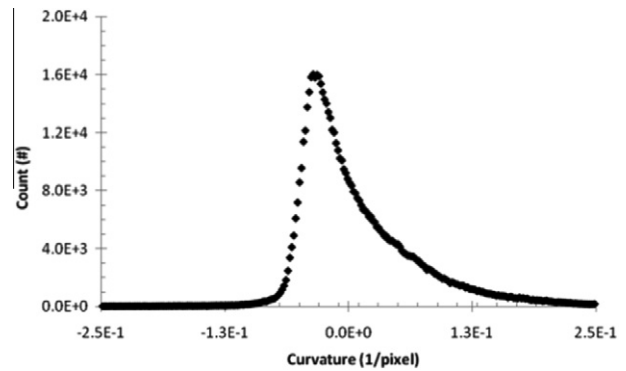

Fig. 2. Distribution of curvature values for the connected phase interfaces, measured on a CMT image for a drainage point. The count is the number of surface elements that have a given curvature value.

are therefore most susceptible to segmentation error. What appear to be correct curvatures are observed in Regions 1 and 2 in the gray-scale image in Fig. 3a, however, after segmentation the interfaces either become flat (e.g. Region 1, Fig. 3b) or curve the wrong way (e.g. Region 2, Fig. 3b). This is also seen in the isosurfaces, see Fig. 3c and d where the curvature values assigned to the surfaces are either zero (Region 1) or positive (Region 2).

Fig. 4 shows that the oil phase is less affected by segmentation error, since residual oil blobs exist as larger features (Fig. 4a) than wetting phase pendular rings (Fig. 4b). The curvature error resulting from inadequate segmentation of small features is clearly displayed in Fig. 4b, where the interface for the pendular ring has become convex rather than concave. In Fig. 5 we present example curvature values measured from a single CMT volume of the disconnected water phase interfaces (i.e. at low saturation). As expected, a single peak curvature value does exist for the collection of pendular rings. However, the majority of the curvature values are positive, and thus, the curvature of the disconnected water phase interfaces at this low saturation are incorrect. The disconnected oil phase interfaces, however, were not affected by the pixilation-related segmentation error; example histograms are provided in Fig. 6 and are discussed in further detail below. To account for segmentation error, the incorrect positive curvature values were removed from further analysis when calculating $\langle P_c \rangle$ from curvature.

3.2. Phase connectivity and residual morphologies

Based on the separation of phases described above (classifying them as 4 different fluid configurations), CMT images were also analyzed for phase connectivity during drainage and imbibition. The existence of disconnected water in glass beads is debatable, since it is likely that water was connected throughout the column via thin films at low saturation. Regardless, disconnected fluid interfaces, identified via this analysis, have significantly different curvature from connected fluid interfaces (as discussed later) and are configured as expected in the pore space. For example, disconnected oil exists as isolated blobs (Fig. 4a) and disconnected water exists as pendular rings (Fig. 4b). Disconnected oil is also configured as larger ganglia that span multiple pores (Fig. 4c); and in some instances disconnected water can be identified as a tri-pendular ring that connects three adjacent pore necks (Fig. 4d).

Curvature distributions for disconnected oil phase interfaces, during imbibition and drainage, are presented in Fig. 6a and b, respectively. These distributions show multiple "peak" pressures for the disconnected fluid interface. Relatively early during
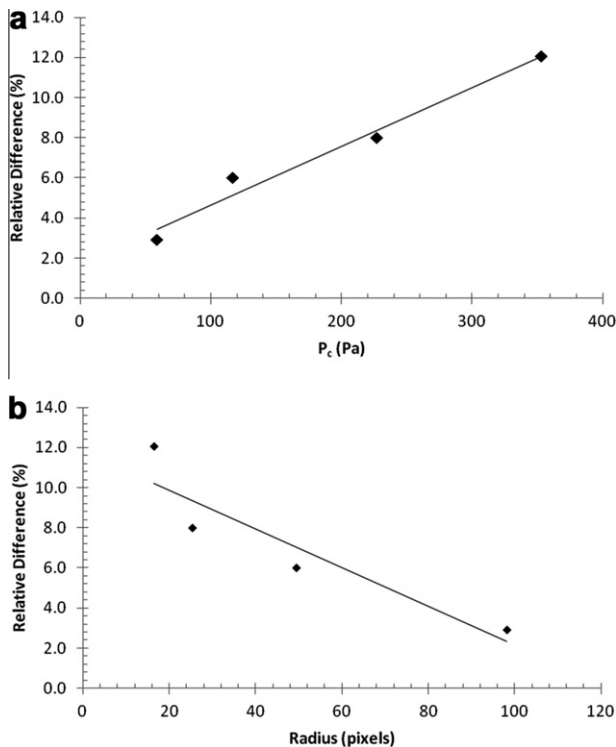

Fig. 1. Error accrued with increasing capillary pressure as estimated based on the artificial CMT capillary meniscus data (a), and as a function of capillary tube radius (b).
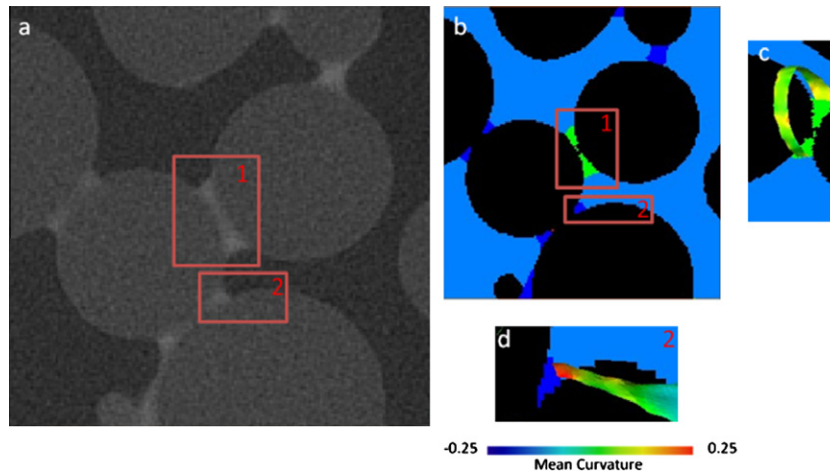
Fig. 3. Example images of segmentation error, regions of interest are labeled 1 and 2 (red boxes). Gray-scale CMT image (a), segmented CMT image (b), connected water phase is dark blue, disconnected water phase is green, and oil is light blue. A pendular ring isosurface is shown in Region 1 (a and b) with incorrect zero curvature (c). A water/oil isosurface is shown in Region 2 (a and b) with incorrect positive curvature (d). (For interpretation of the references to colour in this figure legend, the reader is referred to the web version of this article.)
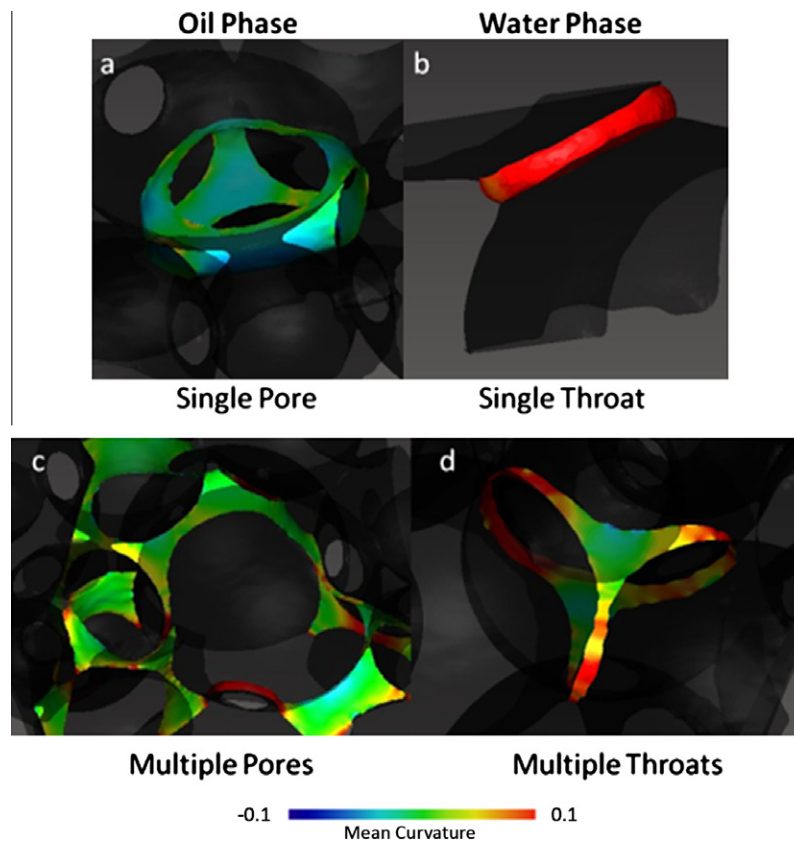
Fig. 4. Example interfacial morphologies, only the isosurface representing the oil/water interface is shown. Disconnected oil blob trapped in a single pore (a). A pendular ring in a single pore neck (b). Large disconnected oil ganglion spanning multiple pores (c). Tri-pendular ring spanning three pore necks (d). The dark transparent phase is the glass beads.

imbibition ($S^w = 0.37$), a small single peak curvature value is present (Fig. 6a) and with increasing saturation, multiple new (and larger) peaks representing lower curvature values appear. Essentially, these "peak" values correspond to the P_c at which the majority of snap-off occurred and the trajectory of these "peak" values in relation to saturation demonstrates that, as imbibition proceeds, disconnected oil blobs with increasingly lower curvatures (i.e. lower P_c) become trapped. The opposite trend is true for drainage

(Fig. 6b) as disconnected oil becomes reconnected; oil blobs with increasingly higher curvatures become reconnected, until close to full oil saturation (low water saturation, $S^w = 0.14$) where only a few high curvature (i.e. large P_c) oil blobs remain. These results suggest that over a short time period (i.e. a time span short enough that interfacial relaxation is not occurring) the curvature distribution of disconnected fluid can be used as a history of P_c values experienced by a system. Additionally, these results show that
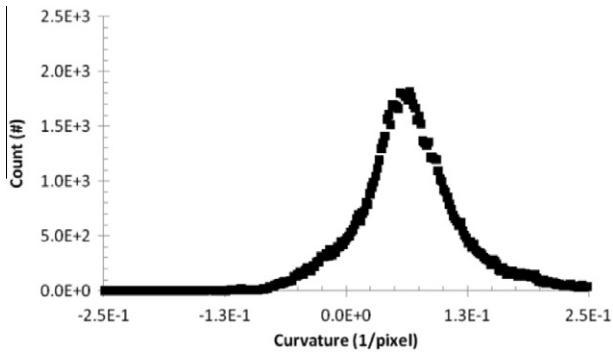
Fig. 5. Distribution of curvature values for the disconnected water phase interfaces as measured from a CMT image, obtained during drainage.

connected and disconnected phase configurations may need to be treated separately, since the pressures and thus internal energies are different. Fig. 6 suggests that we might be able to measure capillary pressure of phases that cannot be probed with an external transducer by measuring curvature from tomographic images, a very exciting prospect for both trapped phase characterization, but also for three-phase fluid systems, where we generally assume that the third trapped phase (gas) remains at atmospheric pressure, partly because we cannot access it with a transducer and provide an alternative value.

During primary drainage, disconnected non-wetting phase was identified. When changing saturation with the syringe pump, the system is in a state far from equilibrium and initially large pressure fluctuations occur (data not shown). We suspect that fluid phase rearrangement occurs during these pressure fluctuations. For example, under drainage, it is likely that both large and small pores are de-saturated, however, once the pump is stopped the smallest pores are refilled with water (re-imbibition) during the initial 10–15 min equilibration time. The occurrence of re-imbibition during equilibration explains why disconnected non-wetting phase is identified during primary drainage and demonstrates that interfacial rearrangement occurs after the pump induced saturation changes are halted (as suggested by Gray and Miller [4]. This disequilibrium is likely caused by a relatively large change in saturation with respect to time prior to stopping the syringe pump which places the system far from equilibrium.

3.3. Capillary pressure measurements

Once the image volumes are segregated into four fluid configurations, the interface formed between connected water and connected oil is readily identifiable. To calculate $\langle P_c \rangle$ from curvature, the average interfacial curvature for connected fluid interfaces was calculated and then related to capillary pressure using Eq. (2). Fig. 7 compares the transducer-based and curvature-based (connected fluid only) capillary pressure-saturation curves. If average curvature for both connected and disconnected interfaces in the CMT image was used to calculate $\langle P_c \rangle$ the results show poor agreement with the transducer-based P^c measurement (see Supporting Material 6), which is another indication that connected and disconnected fluid phases should be treated separately. This is to be expected since the capillary pressure of disconnected fluid is not captured by externally transducer measured P^c. Fig. 7 shows that for drainage, the transducer-based P^c measurement is larger than the curvature-based $\langle P^c \rangle$ measurement; yet, the curvature-based measurement corresponds very well with the transducer-based measurement for imbibition.
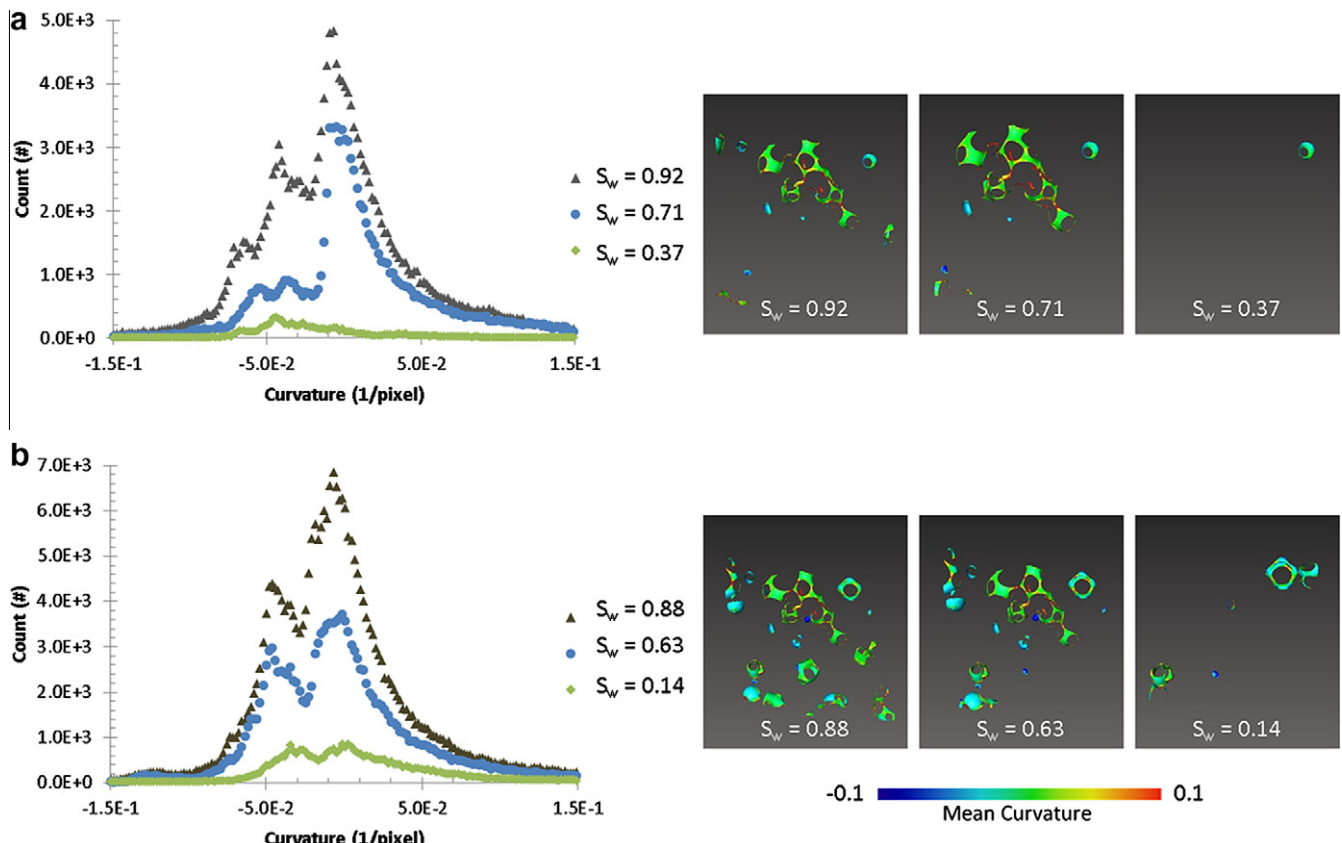

Fig. 6. Curvature distributions for the disconnected oil phase interfaces during imbibition (a) and drainage (b), S^w is water saturation.

We identify three likely causes for the discrepancy between transducer-based and curvature-based capillary pressure values: (1) error in the transducer, (2) error in the curvature estimate due to limited image resolution, and/or (3) disequilibrium effects. The first possible source of error is unlikely since the pressure transducer is accurate within ±0.25%. However, small errors due to the vertical placement of the transducer relative to the sample are possible since this can only be done with mm precision. To explore the second possible source of error we compare transducer-based P^c to curvature-based $\langle P^c \rangle$ (see Fig. 8). A 1:1 line is expected at equilibrium, if our curvature measurement is 100% accurate. The data shows a definite upward trend, suggesting that random error is unlikely; however, systematic error is possible. Since error increases with increasing P_c (Fig. 1) it would be expected that at larger capillary pressure, the measured values would deviate from the 1:1 line. Indeed, measurements obtained during drainage (i.e. higher capillary pressure than during imbition) lie further from the 1:1 line than measurements obtained during imbition. While disequilibrium effects would also cause deviation from the 1:1 line, equilibrium is better evaluated by comparing changes in curvature as a function of equilibration time.

Fig. 9 addresses the third possible source of error and shows that the relative percent difference between curvature-based and transducer-based capillary pressure measurements relative to the average value of these two measurements is dependent on equilibration time. For both drainage and imbition, the relative percent difference between the two measurement techniques decreases as equilibration time increases. While there are some effects due to saturation differences (errors that are more pronounced at higher P_c, as mentioned before, and could be the source of some noise) a consistent trend is obtained with increasing equilibration time (regardless of saturation). Results demonstrate that interfacial relaxation and/or rearrangement is occurring and that $\langle P_c \rangle$ values
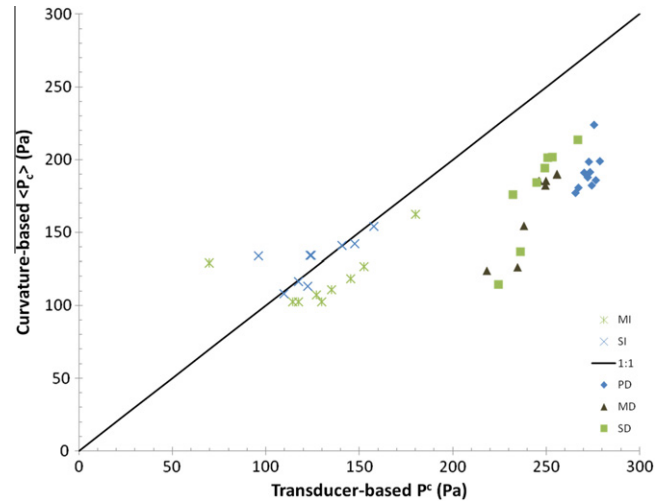

Fig. 8. Transducer-based P^c versus curvature-based $\langle P_c \rangle$ measurements.

calculated from interfacial curvature do not match the P^c values measured by the pressure transducer prior to equilibrium. We observe that drainage equilibration appears to take longer than equilibration during imbition, however, these differences could also be caused by the larger errors associated with the higher curvature values encountered during drainage. Overall, it is hypothesized that longer equilibration time would allow for P_c stabilization and more similar transducer-based P^c and curvature-based $\langle P_c \rangle$ values. The pressure transducer data was also analyzed for equilibration (not shown here) and the data indicates that interfacial relaxation and/or rearrangement was occurring. This suggests that while the fluid pressures in the wetting and non-wetting phases
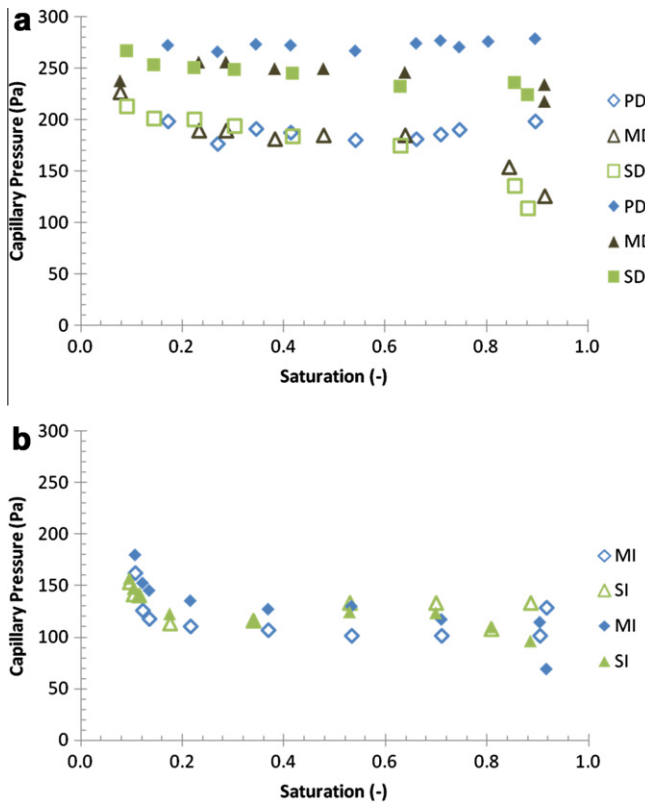

Fig. 7. Capillary pressure saturation curves for drainage (a) and Imbition (b). Curvature-based $\langle P_c \rangle$ (open symbols) and transducer-based P^c (closed symbols).
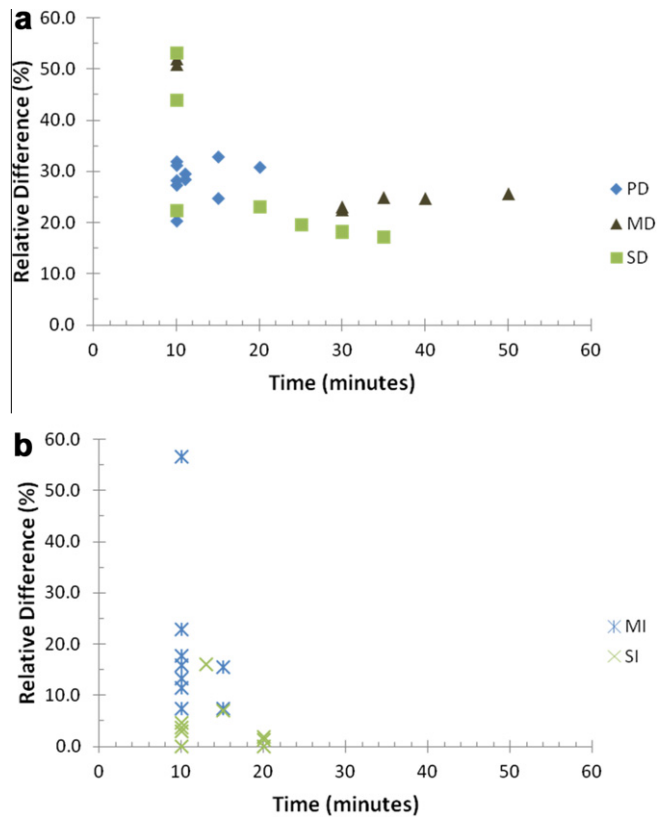

Fig. 9. Relative percent difference between transducer-based P^c and curvature-based $\langle P_c \rangle$ as a function of equilibration time for drainage (a) and imbition (b).

are changing and interfacial relaxation and/or interfacial rearrangement is occurring, as expected the Young–Laplace equation (Eq. (2)) is not valid for this situation and that dynamic effects should be accounted for until equilibrium is achieved. While the rate at which interfacial relaxation occurs and the potential dynamic effects of interfacial rearrangement need further investigation, our data suggests that interfacial equilibration should be considered, consistent with the theoretical results of Gray and Miller [4]. However, for less idealized porous media (and at larger scales) it is likely that the time needed for equilibration would differ from the time needed in the glass bead pack.

4. Conclusions

A method to measure interfacial curvature from CMT images was presented herein. The method was validated by measuring curvature on a few different ideal systems and then used to compare curvature-based and transducer-based capillary pressure measurements during drainage and imbibition experiments. Overall, results between the two capillary pressure measurement techniques agreed well for imbibition near equilibrium ($\sim$10% RPD, if disconnected fluid interfaces are excluded). The transducer-based P^c measurements differed rather significantly from curvature-based $\langle P_c \rangle$ measurements when equilibrium was not reached ($\sim$50% RPD). Further experiments, using longer equilibration times, and facilitating more accurate curvature measurements of the disconnected water phase interfaces via higher resolution images, are needed. Our results are the first to measure interfacial curvature using CMT data, allowing us to explore the capillary pressure saturation relationship from a new perspective, which should fuel further discussion.

Based on the data obtained and analyses performed for this glass-bead pack we can establish the following conclusions:

- Capillary pressure based on curvature and transducer measurements are comparable within $\sim$20% RPD for drainage and <10% RPD for imbibition when >20 min was allowed for equilibration.
- Equilibrium was not reached for some of the early-scan data points (<20 min, Fig. 9).
- Connected and disconnected phases differ in curvature at a given capillary pressure and should be considered separately.
- Curvature measurements can provide useful insights about multi-phase behavior, in particular transitions between dynamic and equilibrium states.
- Higher resolution images (i.e. > $\sim$13 µm/pixel) are required to properly segment small features (in this analysis small features, such as pendular rings, were omitted).
- Additional experiments using longer equilibration times are needed to further address equilibration issues.

Acknowledgements

Appendix A. Supplementary data

Supplementary data associated with this article can be found, in the online version, at http://dx.doi.org/10.1016/j.advwatres.2012.05.009.

References

[1] Cheng JT, Pyrak-Nolte LJ, Nolte DD, Giordano NJ. Linking pressure and saturation through interfacial areas in porous media. Geophysical Research Letters 2004;31(8):4.
[2] Gray WG, Hassanizadeh SM. Paradoxes and realities in unsaturated flow theory. Water Resources Research 1991;27(8):1847–54.
[3] Gray WG, Hassanizadeh SM. Unsaturated flow theory including interfacial phenomena. Water Resources Research 1991;27(8):1855–63.
[4] Gray WG, Miller CT. TCAT analysis of capillary pressure in non-equilibrium, two-fluid-phase, porous medium systems. Advances in Water Resources 2011;34:770–8.
[5] Held RJ, Celia MA. Modeling support of functional relationships between capillary pressure, saturation, interfacial area and common lines. Advances in Water Resources 2001;24:325–43.
[6] Helland JO, Skjaeveland SM. Relationship between capillary pressure, saturation, and interfacial area from a model of mixed-wet triangular tubes. Water Resources Research 2007;43:W12S10.
[7] Hassanizadeh SM, Gray WG. Mechanics and thermodynamics of multiphase flow in porous media including interphase boundaries. Advances in Water Resources 1990;13(4):169–86.
[8] Hassanizadeh SM, Gray WG. Thermodynamic basis of capillary-pressure in porous-media. Water Resources Research 1993;29(10):3389–405.
[9] Hassanizadeh SM, Celia MA, Dahle HK. Dynamic effect in the capillary pressure-saturation relationship and its impacts on unsaturated flow. Vadose Zone Journal 2002;1(1):38–57.
[10] Joekar-Niasar V, Hassanizadeh SM, Leijnse A. Insights into the relationship among capillary pressure, saturation, interfacial area and relative permeability using pore-network modeling. Transport in Porous Media 2008;74:201–19.
[11] Liu Y, Nolte DD, Pyrak-Nolte LJ. Hysteresis and interfacial energies in smooth-walled microfluidic channels. Water Resources Research 2011;47:W01504.
[12] Manthey S, Hassanizadeh SM, Helmig R, Hilfer R. Dimensional analysis of two-phase flow including a rate-dependent capillary pressure-saturation relationship. Advances in Water Resources 2008;31:1137–50.
[13] O'Carroll DM, Mumford KG, Abriola LM, Gerhard JI. Influence of wettability variations on dynamic effects in capillary pressure. Water Resources Research 2010;46:W08505.
[14] O'Carroll DM, Phelan TJ, Abriola LM. Exploring dynamic effects in capillary pressure in multistep outflow experiments. Water Resources Research 2005;41:W11419.
[15] Porter ML, Wildenschild D. Image analysis algorithms for estimating porous media multiphase flow variables from computed microtomography data: a validation study. Computational Geosciences 2010;14(1):15–30.
[16] Porter ML, Wildenschild D, Grant G, Gerhard JI. Measurement and prediction of the relationship between capillary pressure, saturation, and interfacial area in a NAPL-water-glass bead system. Water Resources Research 2010;46:W08512.
[17] Porter ML, Schaap MG, Wildenschild D. Lattice-Boltzmann simulations of the capillary pressure-saturation-interfacial area relationship for porous media. Advances in Water Resources 2009;32(11):1632–40.
[18] Pyrak-Nolte LJ, Nolte DD, Chen D, Giordano NJ. Relating capillary pressure to interfacial areas. Water Resources Research 2008;44:W06408.
[19] Reeves PC, Celia MA. A functional relationship between capillary pressure, saturation and interfacial area as revealed by a pore-scale network model. Water Resources Research 1996;32(8):2345–58.
[20] Stadler AF, Kulik G, Sage D, Barbieri L, Hoffmann P. Colloids and surfaces A: physicochemical and engineering aspects. 2006;286(1–3):92–103, September.